



A genetic algorithm based aerothermal optimization of tip carving for an axial turbine blade

H. Maral^a, E. Alpman^b, L. Kavurmacıoğlu^a, Cengiz Camci^{c,*}

^a Istanbul Technical University, Department of Mechanical Engineering, 34437 Istanbul, Turkey

^b Marmara University, Mechanical Engineering Department, Göztepe Campus, 34722 Istanbul, Turkey

^c The Pennsylvania State University, Department of Aerospace Engineering Turbomachinery Aero-Heat Transfer Lab, University Park, PA, USA



ARTICLE INFO

Article history:

Received 4 October 2018

Received in revised form 5 July 2019

Accepted 13 July 2019

Available online 7 August 2019

Keywords:

Axial turbine

Tip leakage flow

Tip carving

Multi-objective optimization

Genetic algorithm

Artificial neural network

Extreme learning machine

Support vector machine

ABSTRACT

In turbomachines, a properly dimensioned gap between the rotating blade tip and the stationary casing is required in order to avoid mechanical failures due to blade rubbing. Maintaining a tip gap allows the relative motion of the blade, however a leakage flow almost always exists due to the strong pressure differentials existing near the tip airfoil boundaries. Tip leakage flow which is a 3-dimensional and highly complex flow system is responsible from a considerable amount of total pressure loss in a turbine stage. Besides, tip leakage flows induce adverse thermal effects near the blade tip, eventually causing an increase in cooling demand. Various passive control methods exist to weaken the adverse effects of tip leakage flows, in an effort to increase turbine stage efficiency. In this paper, a novel tip carving approach is applied to mitigate the undesired aerothermal effects of the tip leakage flow. A numerical investigation is carried out to obtain the optimum shape of the carved blade tip with an objective function to minimize both heat transfer and leakage loss. A genetic algorithm is used for the optimization, integrated with a meta model which predicts the objective functions quickly. Various meta-models such as Artificial Neural Network (ANN), Extreme Learning Machine (ELM) and Support Vector Machine (SVM) are tested for this purpose. An initial database consisting of 55 blade tip geometries is created for meta-model training using "Sobol design of experiments" methodology. This database is then successively enlarged using a coarse-to-fine approach in order to improve the prediction capabilities of the meta-models. Once a sufficient level of prediction error and a proper consistency is achieved, the optimization process is terminated. Current results indicate that carved blade tip designs are likely to achieve a considerable improvement in aero-thermal performance of axial turbine stages. Multi-objective optimization of the blade tip surface of the carved type is a promising approach in gas turbines since it paves the way for undiscovered blade tip designs for further performance improvements.

© 2019 Elsevier Ltd. All rights reserved.

1. Introduction

The presence of a tip gap between rotating blade tip platforms and the casing induces a non-negligible leakage flow from the pressure side to the suction side. This leakage flow is complex and turbulent and it evolves into a dominant vortical flow structure near the suction side corner of the blade after leaving the gap. Tip leakage vortex also interacts with the passage vortex causing a measurable stage efficiency deterioration. About one third of the overall total pressure losses in an axial turbine stage is due to the tip leakage flow [1]. The leakage flow is also responsible for the reduction in blade aerodynamic loading at blade tip. Besides, the

work extraction ability of a turbine blade decreases since the tip leakage flow is not turned as the passage flow [2–4]. In addition to aerodynamic aspects, tip leakage flows generate excessive thermal loads near blade tip sections. The leakage flow finds itself in the tip gap before doing any significant mechanical work on the rotating blade therefore it carries the maximum possible total temperature level causing severe thermal loads [3–6]. As a result, a cooling method, which brings an additional cost, is required to counteract the adverse thermal effects.

Various methods exist to reduce the undesired effects of the leakage flows. Numerous researchers focused to develop novel geometrical features to improve the aerothermal performance by weakening the tip leakage flow mass flow rate and momentum flux. Several modifications were applied to the blade tip in order to reduce the total pressure loss and the heat transfer to the blade

* Corresponding author.

E-mail address: cxc11@psu.edu (C. Camci).

Nomenclature

A	area of the blade tip, squealer side, and cavity floor	MSE	mean square error
ANN	artificial neural network	NSGA-II	nondominated sorting genetic algorithm 2
CAD	computer aided drawing	\bar{Nu}	average Nusselt number
CFD	computational fluid dynamics	Nu_{FL}	average Nusselt number for flat tip
C_a	axial chord length	P_0	total pressure
$C_{a,27}$, $C_{a,45}$, $C_{a,59}$, $C_{a,77}$	axial planes located perpendicular to the camber line in streamwise direction with respect to the axial chord length	P_{01}	mass flow averaged total pressure at the inlet section
C_p	static pressure coefficient	PS	Pressure Side
C_{p0}	total pressure coefficient	RANS	Reynolds-Averaged Navier-Stokes equations
DOE	design of experiment	SS	suction side
ΔC_{p0}	total pressure loss coefficient, mass flow averaged total pressure coefficient at exit plane	SVM	support vector machine
$\Delta C_{p0,FL}$	total pressure loss coefficient for flat tip	q''_w	wall heat flux
FFNN	feed forward neural network	Re_{inlet}	pU_mC_a/μ
Grid Sensitivity	(GR2-GR1)/GR1(GR3-GR2)/GR2	ρ	density at inlet plane
h	blade height in the linear cascade arrangement	t	tip clearance gap in mm
h	average heat transfer coefficient	TE	trailing edge
k	thermal conductivity of air	T_{01}	mass flow averaged total temperature at the inlet section
LE	leading edge	T_w	wall temperature at the inlet section
LM	Levenberg-Marquardt algorithm	U_m	reference velocity format the inlet of the computational domain
ELM	extreme learning machine	W	wake
MLP	multilayer perceptron		

tip. Squealer and winglet type designs were the most common structures used for this purpose. Heyes et al. [3] showed that partial squealer rims on the suction side of the blade tip surface were capable of reducing the total pressure loss in a linear cascade test rig. A numerical investigation on the effects of squealer designs by Ameri et al. [7] revealed that squealer blade tip mitigated the tip leakage flow while an increase was predicted for the heat transfer rates to the blade tip. Measurements for an axial turbine stage in a rotating rest rig by Camci et al. [8] indicated that partial squealer rims located on the suction side of the blade offered a superior performance than the pressure side squealer. Key and Arts [6] carried a numerical investigation comparing the flow fields for flat and squealer tip designs at low and high speed conditions and obtained that squealer design reduced the aerodynamic loss. Heat transfer and pressure measurements performed in a linear cascade by Newton et al. [9] revealed that squealer designs reduced the heat transfer to the blade tip. It was found in a computational investigation by Krishnanbabu et al. [4] that cavity squealer enhanced the aero-thermal performance. Lee and Kim [10] used oil film techniques to visualize the leakage flow and their measurements revealed that a cavity squealer configuration weakened the tip leakage flow. Lee and Choi [11] also performed an experimental investigation on the effects of tip clearance height for cavity squealer designs in a linear cascade arrangement and obtained that cavity squealer was effective in accomplishing a notable reduction in tip leakage flow. Zhou and Hodson [12] numerically investigated the effects of squealer height and width in regard to fluid flow and heat transfer characteristics. They found that thinner squealer designs offered higher aerodynamic and thermal performance. They also obtained that squealer height had complex effects on the aero-thermal performance. A computational effort on the effects of squealer height and width in a broad range by Senel et al. [13] revealed that complex flow structures due to varying squealer dimensions have substantial influence on the aero-thermal performance. Increasing in the height of squealer and decrease in the width of the squealer tends to improve the aero-thermal performance, however

complex flow structures through the cavity has considerable effects on the overall performance.

Dey and Camci [14] performed measurements for winglet designs in a rotating test rig and found that winglet on the pressure side offered better aerodynamic performance than that of the winglet on the suction side. Zhou et al. [15] studied the effects of winglet designs both numerically and experimentally and obtained that pressure side winglet had higher aerodynamic performance compared to the suction side winglet. They also added that location and shape of the winglet structures had a key role in influencing the aerodynamic performance. A numerical study by Coull et al. [2] indicated that suction side winglet reduced the pressure difference around the leading edge. Cheon et al. [16] conducted an experimental investigation into effects of squealer designs equipped with winglet geometry. Measurements indicated that total pressure loss tends to increase to a certain value with increasing width of the winglet and then to decrease with a further increase in winglet width.

A relatively novel method to control the tip leakage flow is casing treatment. Although casing treatment has a broad range of application in axial compressors, its application to turbines is currently limited. An experimental investigation by Rao et al. [17] revealed that casing surface roughening had the potential to reduce the effects of tip leakage flow. Gumusel [18] performed turbine performance measurements in order to determine the aerodynamic performance gains of casing treatment. He was able to design specific casing patterns that were able to reduce the tip leakage flow rate. Kavurmacioglu et al. [19] performed a numerical computation on the influence of the casing grooves in a linear cascade and found that the triple diverged grooves had the best aerodynamic performance.

Results obtained by Maral et al. [20] and Senel et al. [13] demonstrated that any modification on blade tip surface to mitigate the aerodynamic losses through a rotor blade may lead to measurable increase in heat transfer. Enhancing the turbine aerodynamic and thermal performance simultaneously requires a formal multi-dimensional and multi-disciplinary optimization

approach. Zhang and He [21] explored distinct blade tip designs to control the tip leakage flow by choking the flow through tip clearance. De Maesschalck et al. [22] searched fully carved blade tip designs having superior aerothermal performance. De Maesschalck et al. [23] performed multi-objective optimizations for fully carved blade tips and squealer-like geometries and found that further optimization of blade tip could unveil the great potential of numerous undiscovered designs. Adreoli et al. performed a multi-objective optimization study in order to enhance the aerothermal performance of a cooled turbine blade. They generated rims having arbitrary shape around the cooling holes using a parametric approach. They obtained that optimized tip geometries achieved a considerable reduction in heat flux whereas a relatively smaller improvement was calculated in efficiency [24]. Cernat et al. [25] and Paty et al. [26] carried out experimental and numerical studies for the aerothermal performance of two optimized blade tip designs: a carved blade tip design and a multi-cavity squealer like design obtained using multi-objective optimization techniques. In the first part of their study, a detailed experimental investigation was conducted at a high-speed rotating test rig in order to determine the aerothermal performance of the blade tip designs and numerical predictions were compared to the measurements. In the second part, a comprehensive numerical investigation captured the flow structure through the tip gap. Their investigation to determine aerodynamic and thermal performance revealed that tip shaping was capable of improving the aerothermal performance compared to the flat tip. Deveci et al. [27] searched the optimum squealer dimension to enhance the aero-thermal performance using genetic algorithm integrated with artificial neural network. The complex flow structures inside the cavity due to varying squealer height and width leads to an optimization problem and a multi-objective optimization using NSGA-II (Nondominated sorting genetic algorithm 2) resulted in improved aerothermal performance [28].

Past efforts for the optimization of turbine blade tips revealed a great performance enhancement potential in axial turbines. The current paper aims to obtain improved carved blade tips offering further enhancements in aerothermal performance using an optimization technique based on a genetic algorithm coupled with various meta-models. A randomly formed initial database containing 55 carved blade tips is used for the optimization process. Then, the initial database is enlarged using coarse-to-fine approach at each step. Prediction capability of the meta-models are improved at each step aiming to reduce the prediction errors. In the end, optimization process is terminated at the 5th step once a proper consistency in predictions is achieved and the prediction errors are kept below a certain level. The turbine airfoil, inlet Reynolds number, inlet turbulence intensity, pitch-to-chord ratio, Zweifel coefficient, blade turning, trailing edge thickness, and turbine

airfoil selection are that of our turbine research facility. The simplified linear cascade approach was knowingly selected because of the need to focus on the carved tip surface optimization approach at this stage.

2. Numerical method

The numerical calculations are performed in a three-dimensional, incompressible and fully turbulent flow field using Reynolds-Averaged Navier-Stokes (RANS) equations. A finite volume discretization technique was employed using the general-purpose software, ANSYS CFX 16.0. The RANS based computations are further processed in an optimization effort by comparing three different meta models. These meta models were Artificial Neural Network (ANN) [27], Support Vector Machine (SVM) [28] and Extreme Learning Machine (ELM) [29].

2.1. Computational domain

The numerical computations were performed for a single blade passage having tip clearance of $t/h = 1.35\%$. The computational domain in a linear cascade arrangement is given in Fig. 1. A circumferentially periodic three-dimensional turbulent flow was simulated in a single passage in steady state. In this study the casing is modeled to be stationary. Relative casing motion between the blade tip surface and the casing is known to weaken the tip leakage flow. This is a beneficial influence.

The linear cascade was divided into three main blocks to enable a controlled mesh generation; inlet, rotor and outlet blocks respectively in the streamwise direction. The axial length of the inlet domain was equal to $1C_a$ while it is $2C_a$ for the outlet domain.

2.2. Grid generation and boundary conditions

The whole computational domain consists of 48 blocks. The rotor domain is divided into 46 blocks to pave the way to a controlled mesh so as to capture the complex flow structures through the rotor domain. A multi-block domain allows to use the multi-zone method in the meshing module. The multi-zone method is a blocking approach that uses automated topology decomposition in case blocking topology is available. An H-grid topology together with an O-grid around the blade profile is applied to keep the y^+ values at desired levels and resolve the boundary layers. The mesh size is refined towards the wall in the whole computational domain. Fully hexagonal elements are employed in order to reduce the solution time and increase accuracy. Fig. 2 shows the mesh structure in the tip gap, around the leading edge LE and trailing edge TE at hub and blade tip. The figure also reveals the specific grid growth rate in the tip gap such that the gradients are captured

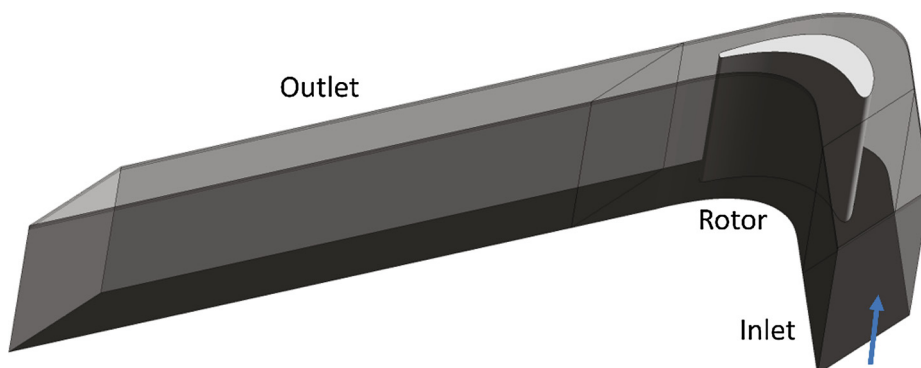


Fig. 1. Computational domain as a linear cascade.

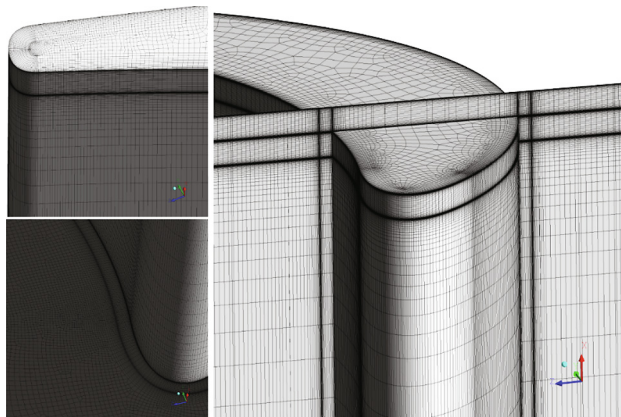


Fig. 2. Fully hexahedral mesh for the flat tip, leading edge and trailing edge.

accurately. In addition to the outer O-grid, a similar structure is formed at the inner region of the blade profile as seen in Fig. 2. A parametric approach is followed in the computations to reduce the time to obtain the results. The current mesh in Fig. 2 involves a double refinement zone due to block structure that paves the way for various blade tip designs of having different dimensions.

The velocity profile in the spanwise direction and the total temperature are defined as the inlet boundary conditions. The mean velocity at midspan is calculated to be 15.4 m/s and the total temperature is 323 K at the inlet of the computational domain. Inlet Re number (Re_{inlet}) based on the axial chord is 103,230. Static pressure and temperature conditions are imposed at the exit of the linear cascade. A turbulence intensity of 1% is specified as an inlet boundary condition. Since the maximum Mach number throughout the computational domain is less than 0.3, the compressibility effects can be neglected. Maximum Mach number in the tip gap is around 0.15. No-slip and temperature boundary conditions are imposed on the solid walls of the cascade. A periodicity condition is introduced in the pitch-wise direction for computations in a single-blade-passage. The flow is assumed to be fully turbulent, thus transitional effects are not taken into consideration in turbulence modeling. A two-equation model of turbulence, Shear Stress Transport (SST) is used in the calculations. SST turbulence model requires that the y^+ values should be kept around 1 since the model is a combination of ($k-\epsilon$) and the ($k-\omega$) turbulence model based on the distance from the wall [29]. In this study, the average y^+ around the blade profile at the blade tip is calculated as 0.7. Thus, the y^+ requirement for the SST model is satisfied. The mesh expansion ratio was 1.2.

Convergence criteria for momentum, energy and turbulence level is specified to be smaller than 10^{-4} . Furthermore, additional variables are monitored for convergence control. Total pressure at a selected point in the tip gap, which is exposed to highly rotational flow is monitored. The total pressure difference at this point of the gap is monitored between two subsequent iterations. The difference in relative total pressure with respect to atmospheric value is less than 0.1% after 100 iterations, once the convergence criteria is satisfied.

2.3. Mesh sensitivity

A mesh dependency test including 3 different mesh measures was carried out for flat tip. The mesh resolution was increased gradually from the so called GR1 to GR3. The mesh dependency study was summarized in Table 1. Mesh size was changed gradually. First layer thickness was changed in mesh sensitivity. Apart from the first cell height, the other sizing parameters were adjusted in a controlled manner. Mass -averaged total pressure coefficient at exit plane (ΔC_{p0}) and the area averaged heat transfer coefficient (\bar{h}) were taken into consideration for the mesh dependency study. Difference in ΔC_{p0} was reduced below 1% for GR3 due to the gradual refinement in the mesh structure. Calculations for the \bar{h} reveals that the difference in \bar{h} also tends to decrease with grid refinement. The variation in \bar{h} with respect to the previous mesh structure is kept below 1%.

Effects of the mesh resolution on the static pressure and heat transfer distribution at blade tip are also investigated. Static pressure coefficient distribution on the blade tip given in Fig. 3 depicts that low-pressure region downstream of the pressure side expands from GR1 to GR3.

The difference due to mesh resolution has been reduced considerably between the GR2 and GR3. Moreover, heat transfer characteristics on the blade tip surface seems to be similar by the refinement in the mesh resolution. Numerical calculations indicate that the mesh dependency is progressively reduced when moving from GR1 to the finest mesh GR3. GR3 was used throughout the study.

2.4. Geometry generation

Exploration of carved tip geometries using a multi-objective optimization algorithm requires large number of designs based on the number of parameters to define the carved blocks that will be removed from the blade tip surface. Parametric definition of the carved blocks using Bezier points enables the user to obtain smooth surfaces to form the carved block. Bezier points are utilized to define the cross-section from downstream of the PS to the upstream of the SS as seen in Fig. 4. The region to be carved occupies the region between 30% axial chord length to 70% between the LE and TE of the blade. The initial location of the planes to form the carved block is determined from the leakage flow rate distribution in streamwise direction as a starting point. The results indicate that re-location of these planes are crucial for the aero-thermal performance. Inside this region the control points are located on three control sections which are almost perpendicular to the camber line of the blade. Each section contained five control points as shown in Fig. 4. In this task, the location of the first and the last control points are kept fixed while the three control points in between are allowed to move along the spanwise direction. This motion restriction was applied in order to avoid large number of design parameters. As a result of this the surface to be carved was defined using a total of nine design variables. The control points were allowed to move in the spanwise direction in such a way that the tip clearance t in Fig. 4 remains unchanged. The maximum

Table 1
Mesh dependency study for the flat tip.

Grid	Number of elements	ΔC_{p0}	Difference in ΔC_{p0} (%)	$\bar{h} [\text{W/m}^2 \text{ K}]$	Difference in \bar{h} (%)
GR1	6,103,486	-0.5491	-	193.1	-
GR2	7,620,603	-0.5663	3.13	194.5	0.73
GR3	9,069,282	-0.5700	0.65	195.3	0.41

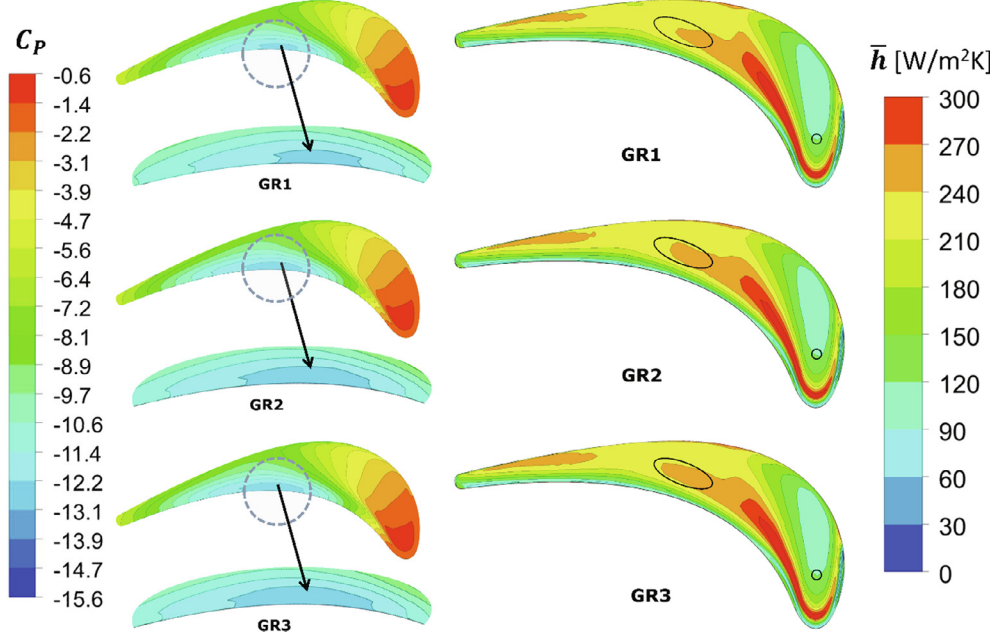


Fig. 3. Mesh dependency study for GR1 to GR3: C_p and \bar{h} distributions on the blade tip.

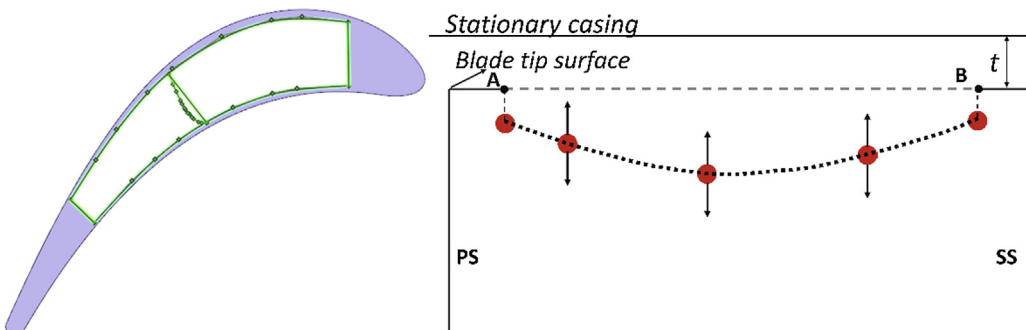


Fig. 4. Parametric definition of carved block section.

allowable depth of the carving process was not allowed to exceed twice the tip clearance t .

Fig. 5 illustrates the formation of the carved blade tip designs. Parametrically defined blocks are carved from the blade tip surface. **Fig. 5** reveals that tip carving approach generates a squealer-like design with a non-flat base. Constraints in the parametrization step are introduced such that instead of removing the whole surface surrounded by the PS and the SS, carving is applied to the region between the PS and the SS excluding PS and SS boundaries. The carving is performed between the points A and B. The height of the top carved block at PS, SS, LE, and TE boundaries is kept at 0.5 mm in order to avoid any problems in mesh generation. The thickness of the surrounding squealer is determined by the control points obtained after optimization procedure. The four control points on the prescribed planes (the first and the last planes) are fixed on the blade tip surface.

As it would be practically impossible to couple the optimization code directly with the CFD solver, a suitable meta-model was used for objective function "total pressure loss coefficient" (ΔC_{p0}) and "heat transfer coefficient" (\bar{h}) predictions. These models require a database of solutions to be trained. The suitable size of the database is very difficult to obtain [24] because there is no specific

theoretical relation for that matter and other than a few rules of thumb. However, based on the number of design parameters to define the carved block an initial database size of 55 is selected. This number is the database size required to fit a 2nd order parabolic response surface to a function with nine variables [30]. The design parameters of the geometries in the database are selected using the Sobol design of experiment (DOE) method [30]. Once the initial database is formed, the mesh generation and CFD solutions are performed for all of the geometries it contains.

2.5. Mesh generation for carved blade tips

The non-conformal mesh interface is utilized for CFD simulations in order to reduce the computational cost and time. Although the non-conformal mesh structure is less orderly and somewhat unstructured, it is the most convenient way of gridding a highly three-dimensional grid geometry. The non-conformal mesh interface technique for carved blocks offers a great convenience in mesh generation by achieving a significant reduction in time. **Fig. 6** shows the mesh for the carved block on the upper and non-conformal mesh interface at the bottom of the figure.

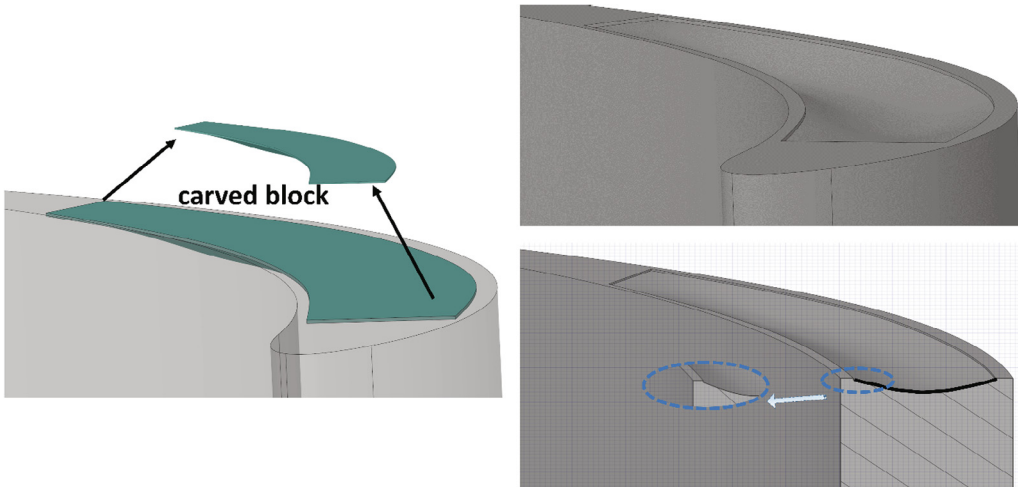


Fig. 5. Blade tip carving approach: removal of the carved block (left) and solid model of the carved blade tip.

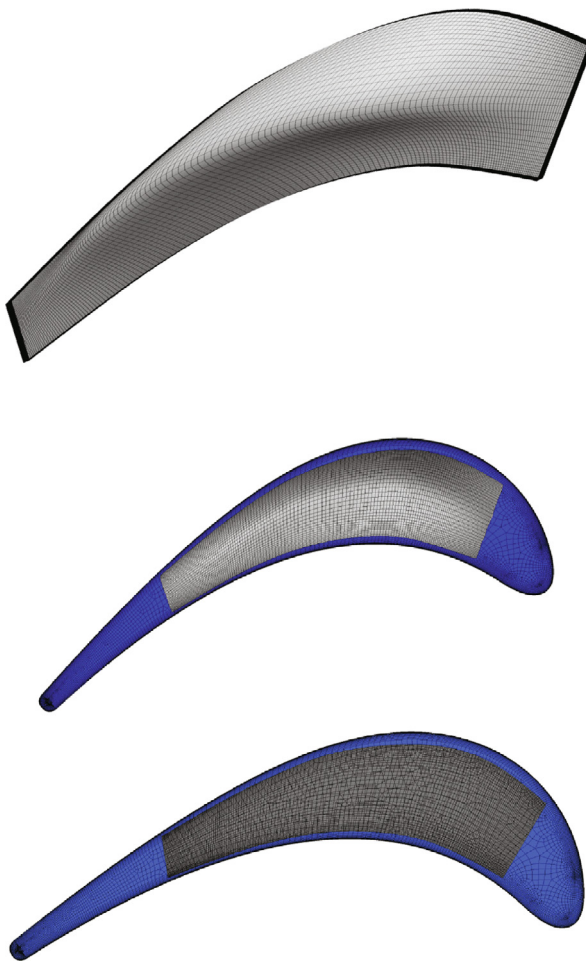


Fig. 6. Fully hexahedral mesh for carved block and the non-conformal mesh interface.

Fig. 7 represents the aero-thermal performance predictions of the carved blade tip designs of the initial database. Total pressure loss coefficient as an objective function is defined as: mass - averaged of total pressure coefficient at the exit plane located one axial chord (C_a) downstream of the trailing edge. The exit plane placed between the hub and casing is located normal to the axial direction of the linear cascade arrangement:

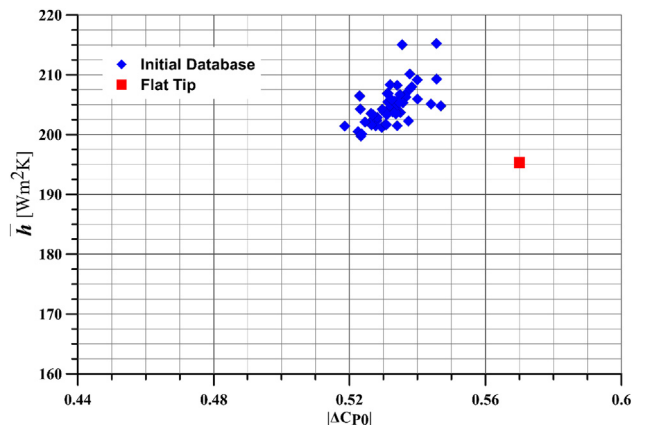


Fig. 7. Aero-thermal performance of the carved designs at initial database.

$$\Delta C_{p0} = \frac{\int \rho u C_{p0} dy dz}{\int \rho u dy dz} \quad (1)$$

where C_{p0} represents the total pressure coefficient which is defined as follows:

$$C_{p0} = \frac{p_0 - p_{0i}}{0.5 \rho U_m^2} \quad (2)$$

p_{0i} is the mass flow averaged total pressure at the inlet of the computation domain and U_m denotes the averaged velocity at the inlet domain. The second objective function is the heat transfer coefficient and calculated as follows:

$$h = \frac{q''_w}{T_w - T_{0i}} \quad (3)$$

where q''_w represents the wall heat flux, T_w is wall temperature and T_{0i} is mass flow averaged total temperature at the inlet of the cascade. Average heat transfer coefficient \bar{h} is defined as follows:

$$\bar{h} = \frac{1}{A} \int h dA \quad (4)$$

The integration area includes all heat transfer surfaces contained in the airfoil boundary of the tip section for the carved blade tip and flat tip. The aero-thermal performance of the blade with flat

tip is also added for reference. Numerical calculations show remarkable dependency to the specific character of the carving. Carved designs offer a notable improvement in aerodynamic performance compared to the flat tip. Unlike the aerodynamic performance, slightly higher heat transfer coefficients are calculated for the carved designs. CFD predictions in general show that minimizing the aerodynamic losses and convective heat transfer rates "simultaneously" may not be possible in a complex multi-objective optimization problem.

2.6. Finding a suitable database size for multi-objective optimization via genetic algorithms

Insufficient number of the solutions in the database to poor prediction capability of the meta-model used and as a result the optimization results would be misleading. Therefore, once the optimization is performed using the initial database, several designs are selected from the obtained Pareto front and CFD solutions are performed for these geometries in order to compute the error between the CFD and meta-model predictions. After this step, these new CFD solutions are added to the database and the process is repeated with the enlarged database. This, iterative procedure is followed until the error between the CFD and meta-model predictions becomes small enough. The initial database was enlarged using a coarse-fine approach since the number of the points required to keep the predictions of the meta-models are not known exactly. Thus, the initial database was decided to be enlarged gradually by adding to 2 points at each step. The optima was indicated in Fig. 8.

In this study, three different meta models were tested and compared with each other for their regression capabilities. These were Artificial Neural Network (ANN) [31], Support Vector Machine (SVM) [32] and Extreme Learning Machine (ELM) [33]. The ANN was a feed-forward neural network (multi-layer perceptron, MLP) consisting of one input layer, one hidden layer and one output layer. The number of layers in the input neuron was equal to 9, the number of design parameters. Since separate networks were constructed for each objective (this is also true for SVM and ELM) the output layer had a single neuron. The number of neurons in the hidden layer was changed between 1 and 50. For each number of neurons, the network is trained and tested 10 times, and the network yielding the smallest testing error was selected as the model. Here, the testing error was calculated as the root mean square of the difference between the test data and network predictions. During the network construction process 80% of the database was used for training, and 20% was used for testing purposes. All networks are trained with Levenberg – Marquardt (LM) algorithm by using the neural network package of the open source scientific programming language GNU Octave [34].

For the SVM, the Matlab/Octave library LIBSVM [32] was used. Here the nu-SVR version, which is suitable for regression, is constructed with a radial basis function kernel was adopted. For the ELM, the network structure was identical to the ANN described above along with the same percentage of training and testing data. However, since the training of ELM was much faster than that of ANN, the number of neurons in the hidden layer was changed

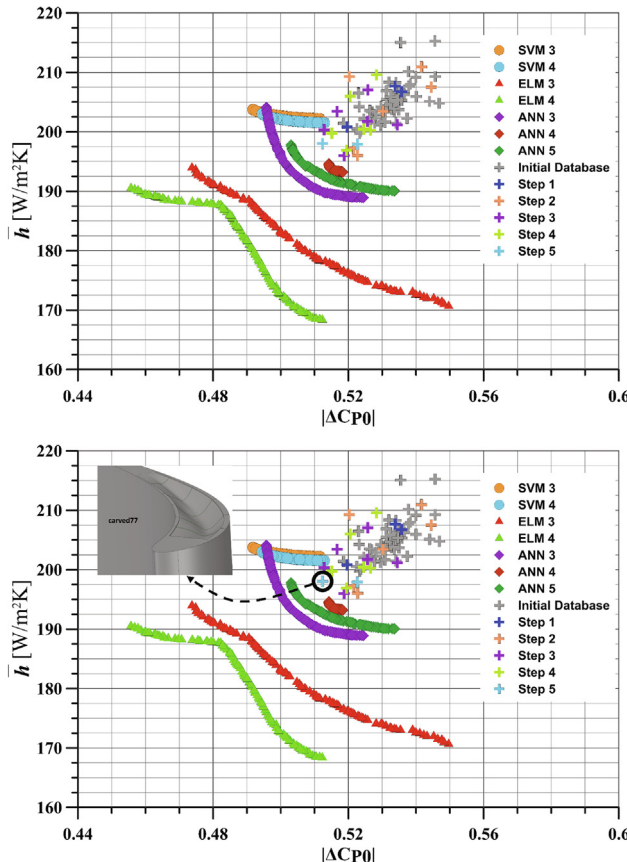


Fig. 8. Pareto fronts and evaluation of the database.

Table 2

Summary of the multi-objective optimization.

Step	Meta-model	Design	CFD results		Meta-models prediction		Difference (%)	
			ΔC_{p0}	\bar{h}	ΔC_{p0}	\bar{h}	ΔC_{p0}	\bar{h}
Step 3	ELM	carved65	-0.5167	203.4	-0.4737	193.9	8.31	4.67
	ELM	carved66	-0.5345	201.2	-0.5354	173.0	-0.17	13.98
	ANN	carved67	-0.5188	196.0	-0.5244	188.9	-1.09	3.61
	ANN	carved68	-0.5128	200.3	-0.4957	204.1	3.34	-1.91
	SVM	carved69	-0.5258	207.0	-0.4918	203.8	6.46	1.58
	SVM	carved70	-0.5256	201.7	-0.5116	202.2	2.68	-0.23
Step 4	ANN	carved71	-0.5151	199.7	-0.5143	194.6	0.16	2.57
	ANN	carved72	-0.5195	196.9	-0.5184	193.2	0.21	1.88
	SVM	carved73	-0.5245	200.4	-0.5129	201.5	2.22	-0.55
	SVM	carved74	-0.5206	206.0	-0.4945	203.0	5.01	1.44
	ELM	carved75	-0.5283	209.6	-0.4557	190.5	13.75	9.11
	ELM	carved76	-0.5266	200.2	-0.5123	168.3	2.71	15.93
Step 5	ANN	carved77	-0.5123	198.0	-0.5030	197.8	1.82	0.11
	ANN	carved78	-0.5227	197.9	-0.5336	190.0	-2.09	3.96

between 1 and 100 and for each case, the network was trained 50 times. Again, the network which yielded the minimum testing error was picked for the optimization studies.

3. Results and discussion

In this study, the optimization procedure was repeated 5 times by increasing the number of the points in the database as described in the previous section. Table 2 indicates the carved blade tip designs obtained from the Pareto-front at each step excluding the Step 1 and Step 2. Here, step 1 and 2 are not displayed in this table because of an improvement made on the heat transfer coefficient calculations after the second step. Since the improvement was applied during post-processing it did not affect the already obtained CFD predictions however the designs added to the database would not be really on the Pareto front of that step. Since the added points in step 1 and 2 would improve the database regardless of their being on the Pareto front or not, they were decided to be kept for the oncoming steps. The meta-model predictions and the deviation from the CFD results of each meta-model

are also listed in the table. Results indicate that prediction capabilities of the meta-models were improved due to the enlarged database except for the ELM. Prediction errors of ELM were quite high even though the database becomes larger at each step. Compared to the ELM the difference between the CFD results and predictions of ANN and SVM was smaller. However, ANN was found to offer the best performance in the prediction of the fitness functions. Therefore, only ANN was used in the last step.

Fig. 8 represents the Pareto-fronts obtained at each step by all meta-models and the evolution of initial database. The x- and the y-axes denote the absolute value of the mass flow averaged total pressure loss coefficient and averaged heat transfer coefficient at the blade tip surface, respectively.

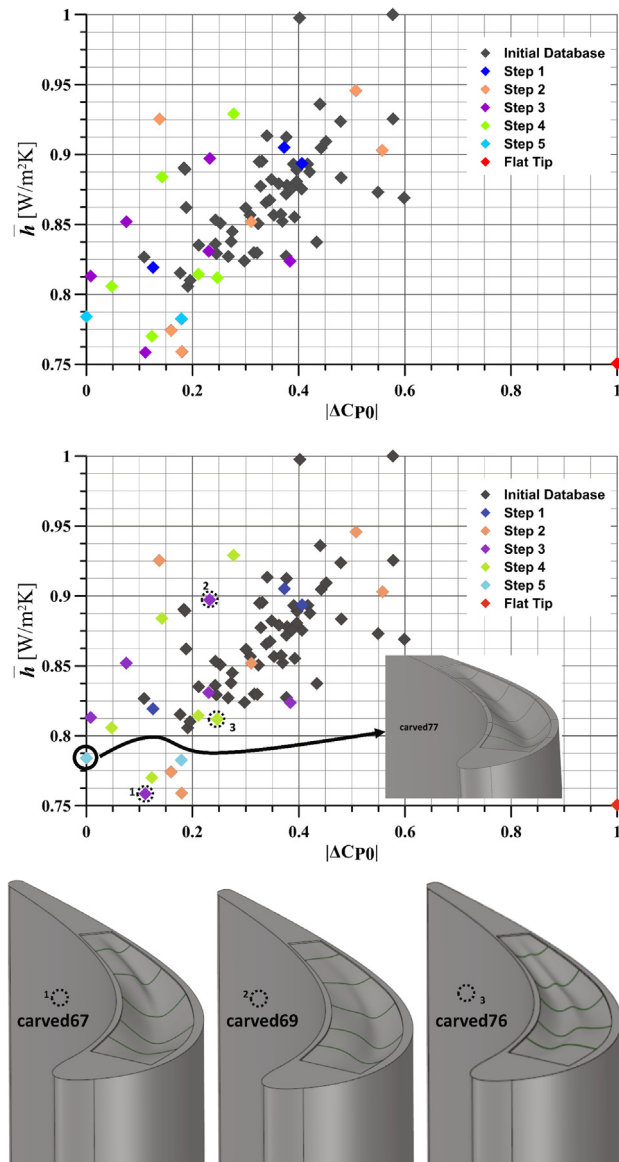


Fig. 9. Extended database at each step compared to the flat tip and three viable designs.

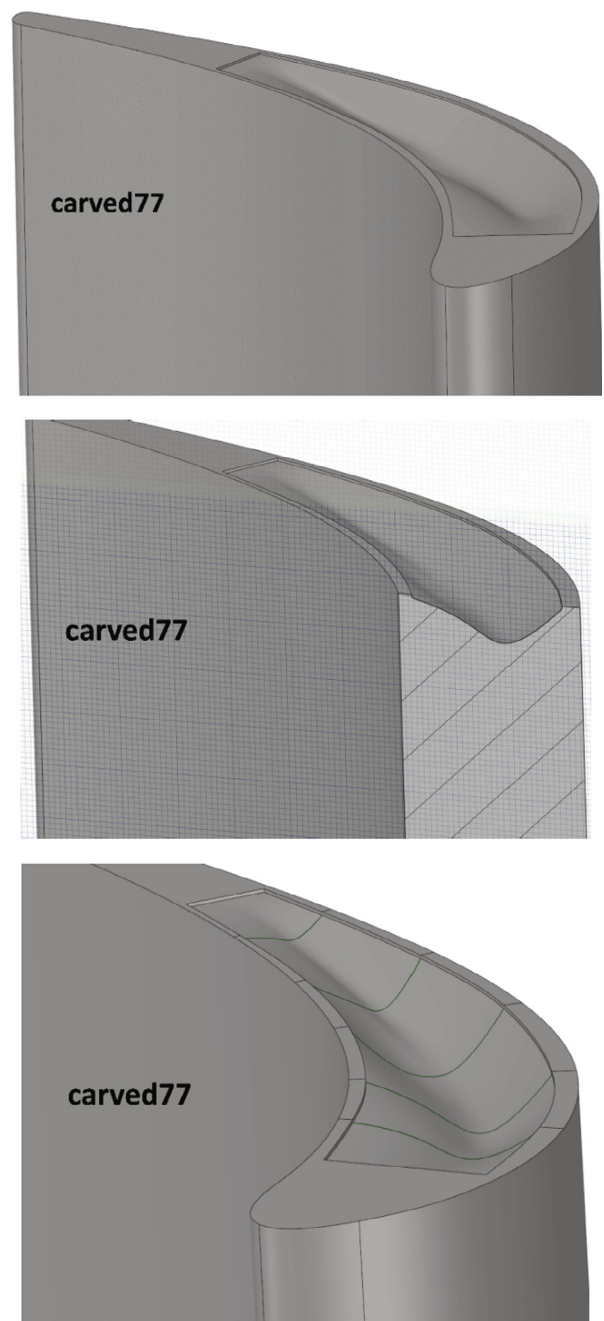


Fig. 10. Optimized blade tip design obtained from the current multi-objective optimization method, carved77 solid model and cross-sectional view.

Pareto fronts look significantly different from one strategy to the other. The training process of each model is different from each other. As a result, predictions and prediction errors show various characteristics. Fig. 8 includes the Pareto fronts representing both meta-model predictions and the CFD results. The meta-model prediction errors never became zero. Thus, for any point meta-model prediction and the CFD result will not coincide in the figure.

Pareto-fronts yielded by the NSGA-II algorithm coupled with the meta-models reveal that ELM converged the origin of the graph faster than ANN and SVM. However, ELM had a poor prediction capability with respect to other meta-models, the predictions displayed in Fig. 8 were not in good agreement with the CFD predictions. This clearly showed how misleading the optimization results could be if an accurate metamodel was not employed.

Results also indicated that ANN and SVM seem to be more consistent than ELM. Fig. 8 indicated a slight difference between SVM 3 and SVM 4 Pareto-fronts. Averaged heat transfer coefficient predictions of SVM did not decrease below a certain level whereas SVM offered a wide range for the total pressure loss. Similar to SVM, ANN predictions were also considered to be consistent. It is worthy to note that Pareto front obtained at step 5 by ANN lied between ANN 3 and ANN 4 fronts. As a result, it can be concluded that ANN predictions converged to a certain front.

The progress of database through the optimization steps are demonstrated in Fig. 9. The axes contain the normalized values of the objective functions. The aerothermal performance of the blade with flat tip is also added as reference. According to Fig. 9, the designs close to the lower left corner of the graph have higher aerothermal performance with minimum loss and heat transfer coefficients. It is evident that points added to the database gradually extend it towards the corner of the graph. Therefore, it

is evident that the multi-objective optimization procedure used enabled to improve the aero-thermal performance of the blade.

Fig. 9 clearly indicates that flat tip is one of most distant designs to the corner. However, it should be emphasized that the flat tip cannot be dominated by any point in the enlarged database due to having the least heat transfer coefficient. Non-domination is one of the crucial points in multi-objective optimization. In addition to non-domination, quantification of the aero-thermal performance is another key point to make a comparison between the designs. The individuals on the Pareto-front represent the best performing designs without dominating each other. The designer can select any of them depending on the requirement, operational conditions.

Results indicate that it may not be feasible to develop a blade tip design having the best aerodynamic and thermal performance simultaneously. Design specifications result in a decision problem. In a simple way, the designer can introduce weight functions in order to bring a solution to this problem. In this study, it was found that changing the weight functions led to different carved designs. For instance, weighting the objective functions equally results in the so-called carved67 design (see Table 2) while assigning the weight functions to be 60% and 40% for aerodynamic and thermal aspects respectively leads to carved77 design. In this study, the carved77 design was chosen to proceed with further investigations because aerodynamic losses were considered to be more important than the heat transfer field by a specific design request.

Fig. 10 shows the optimized blade tip design obtained from the current multi-objective optimization method. Squealer-like tip carving resulted in improved aero-thermal performance. Total pressure loss coefficient (ΔC_{P0}) at the exit plane located one axial chord downstream of the trailing edge is shown in Fig. 11. C_{P0}

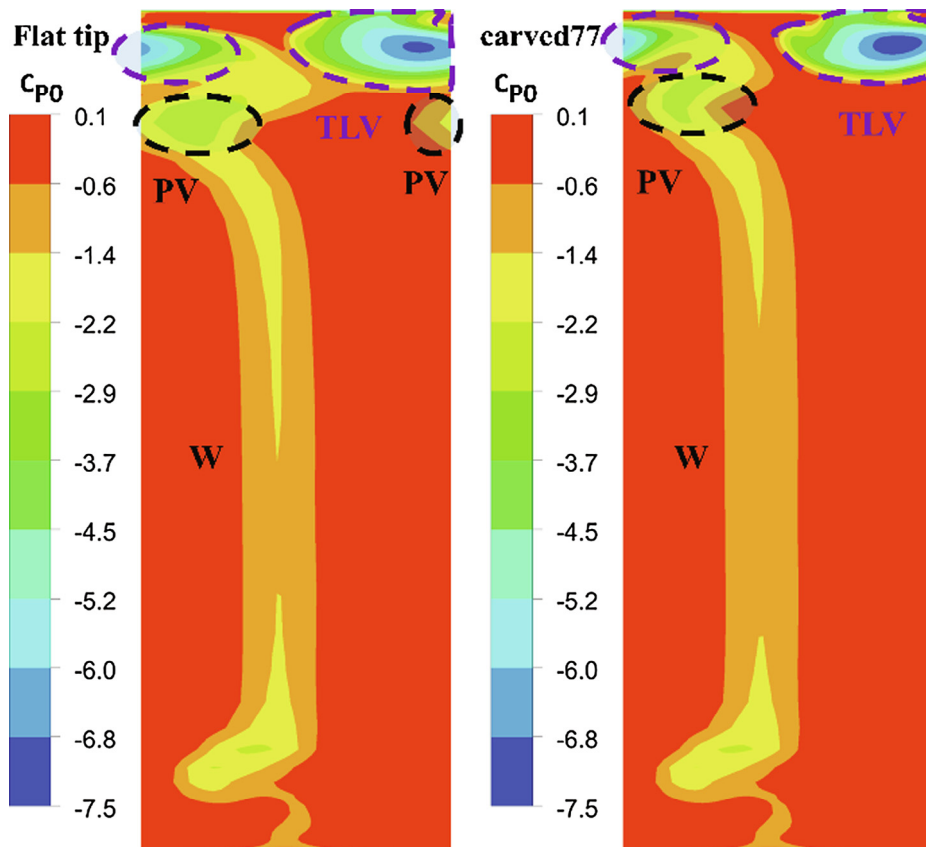


Fig. 11. C_{P0} distribution at the exit plane located downstream of the trailing edge.

distribution indicates that carved77 design improved the aerodynamic performance by weakening both the tip leakage vortex (TLV) and the passage vortex (PV). The passage vortex (PV) originates from the fact that there is a momentum deficit in the incoming endwall boundary layer (casing and hub). The severe turning of the inlet endwall (casing) boundary layers in the rotor passage results in the formation of a passage vortex. The passage vortex also includes the remnants of the horse-show vortices originating from the leading edges of the blade airfoils near the casing and hub.

Tip carving reduced occupation area of the TLV and PV considerably. However, the loss in the core of TLV becomes slightly higher for carved77 design. The usual aerodynamic interaction between TLV and PV for the flat tip design is measurably reduced by tip carving.

Streamlines released upstream of the leading edge reveals that carved blade tip design diverted the tip leakage flow through the cavity. As a result, the lower leakage flow rate was calculated for the carved77 design. Optimized carved blade tip achieved 11.5% reduction in leakage flow rate. Fig. 12 also indicates that the tip leakage vortex moves towards the suction side of the blade. The leakage vortex which comes closer to the SS can reduce the leakage flow by blocking the leakage flow. The LV spreads over a smaller area for carved77 design compared to the flat tip. Despite the

reduction in leakage flow rate and size, the leakage vortex core occupies a relatively larger area. A weaker passage vortex is predicted in the carved design as seen in Fig. 11. Squealer-like tip carving effectively modifies the tip leakage vortex and passage vortex formation.

Heat transfer coefficient on the blade tip surface is plotted in Fig. 13 together with velocity vectors on axially located planes. High heat transfer region around the leading edge is due to the vortex pair impinging on the blade tip surface. Incoming flow over the leading edge impinges on the tip surface and forms a vortex similar to horseshoe vortex. The pressure side arm of the vortex pair impinges on the cavity bottom surface. The depth of the cavity near the pressure side is not sufficiently high to avoid high heat transfer to the bottom surface of the carved tip as seen in Fig. 13. Incoming flow over the leading edge impinges on the uncarved/untreated part of the blade tip surface causing higher thermal loads around the blade leading edge. Since the leakage flow re-attaches on the bottom surface, high heat transfer is calculated. Velocity vectors projected on the axially located planes shows vortical structures inside the cavity. These vortical flow structures inside the cavity act as relatively low thermal transport areas, therefore lower heat transfer coefficient is predicted. Although there are impingement zones, a good portion of the bottom surface interacts with separated low momentum zones. The leakage flow passing over the

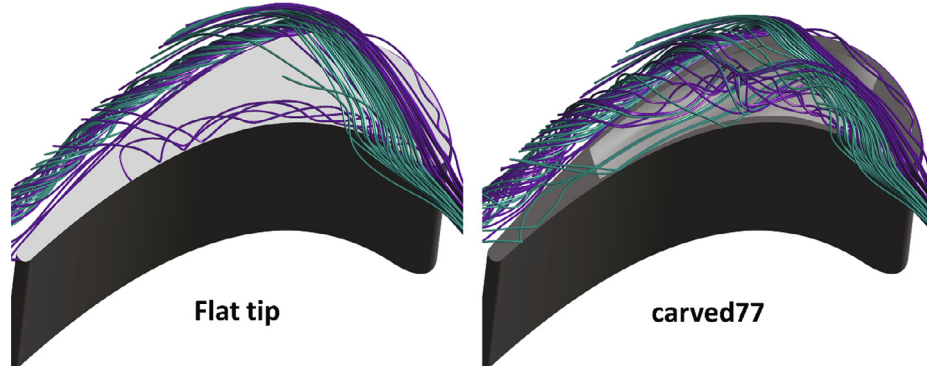


Fig. 12. Streamlines in the tip gap released upstream of the leading edge.

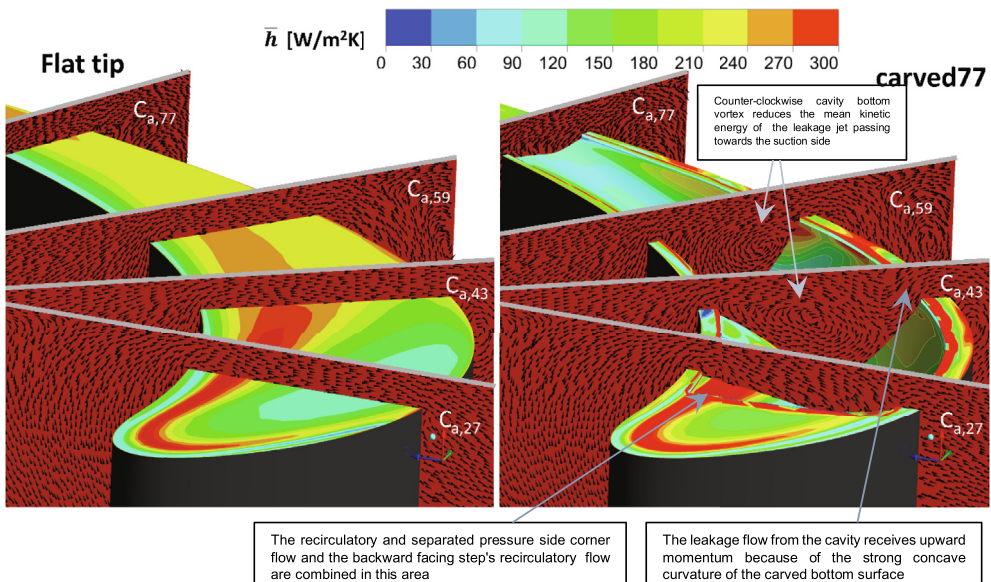


Fig. 13. Velocity vectors in the cavity and the corresponding heat transfer coefficient distribution on the curved bottom surface.

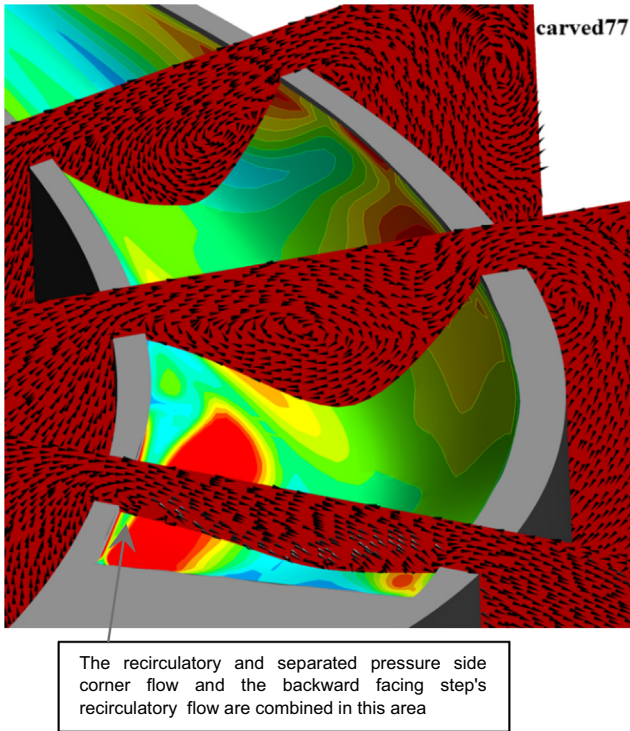


Fig. 14. High heat transfer region due to the impingement of the leakage flow.

cavity vortex impinges on the bottom surface of the cavity near the suction side. Velocity vectors impinge on the surface represent the high heat transfer region.

Tip carving reduced the heat loads on certain parts of the blade tip. Slightly higher heat transfer is calculated for the carved77 downstream of the pressure side and upstream of the suction side. The height of the carved block near the pressure side seems to be not enough since the incoming flow over the leading edge

impinges on the surface. The leakage flow leaving the tip gap impinges on the suction side of carved block. Increase in the average heat transfer coefficient is due to the geometric definitions of the carved block. Results show that geometrical constraints in defining the carved block can be adjusted to improve the thermal performance. Fig. 14 represents a magnified view of the heat transfer coefficient distribution on the cavity bottom surface. The leakage flow in certain areas interacts with the surface in a complex way causing higher heat transfer to the tip surface. Thermal transport in impingement influenced areas are enhanced. Velocity vectors visualized in the middle plane of Fig. 14 show that the leakage flow follows the concave cavity surface instead of impinging on it. This type of flow structure is likely to reduce the thermal loads to the compound-curved bottom surface. The curvature of this bottom surface provides an upward momentum to the leakage jet moving towards the suction side corner. This additional upward momentum induced by tip carving is one of the reasons for reduced leakage mass flow rate.

There are three vertical planes in Fig. 13 visualizing the three-dimensional and highly re-circulatory motion of the tip gap. This figure shows the great influence of the re-circulatory flow induced by the curved bottom surface of the carved tip cavity. The recirculatory motions are somewhat limited just downstream of the leading-edge boundary of the carved cavity. The heat transfer on the bottom cavity shows the influence of the leading-edge vorticity as shown in the red areas of Figs. 13 and 14. The straight LE boundary of the carved cavity generates a highly visible heat transfer zone near the pressure side corner of the cavity. The backward facing step originating at the straight LE boundary of the cavity and the leakage jet starting to form near the PS corner combine their influences to define this high heat transfer zone (red). The recirculatory/separated pressure side corner flow and the backward facing step's recirculatory corner flow are combined in this area. The middle vertical plane shows a highly recirculatory flow system. The leakage flow in the cavity has a dominant clockwise vortical system covering almost all of the bottom curved surface of the carving area. The high momentum leakage jet near the casing boundary

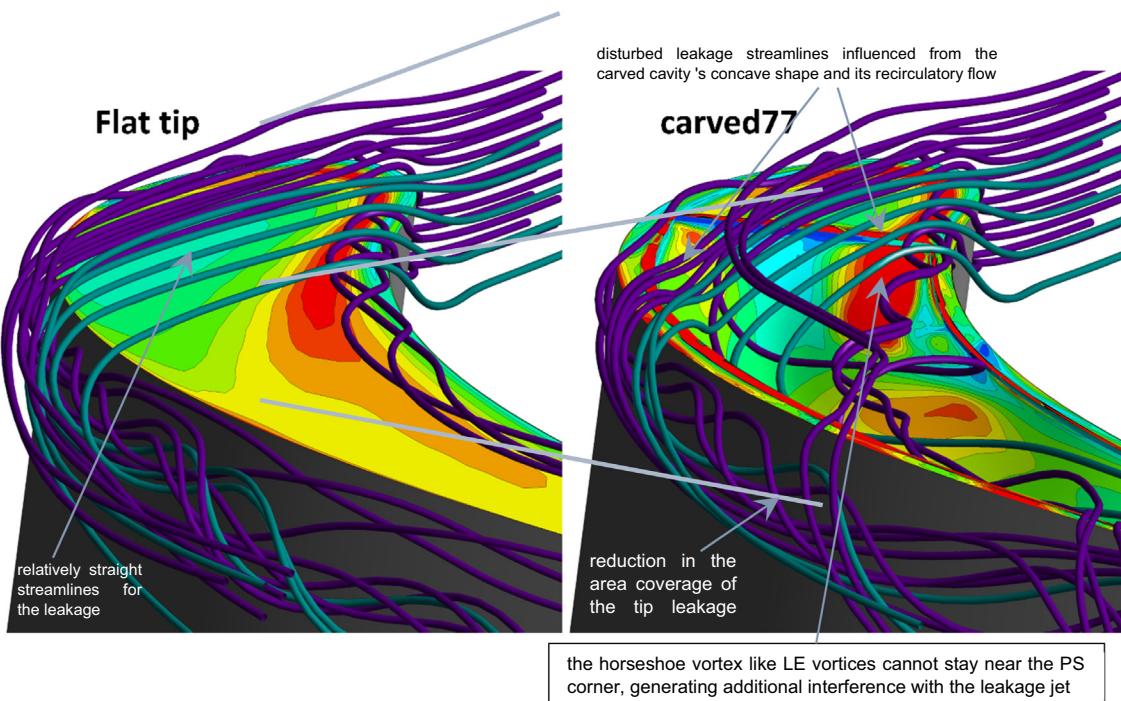


Fig. 15. Heat transfer coefficient distribution on the blade tip surface along with velocity vectors at C_a planes and the influence of the carved tip cavity on the leakage streamlines.

usually shoots towards the suction side rim for a regular squealer tip design. Counter-clockwise cavity bottom vortex reduces the mean kinetic energy of the leakage jet passing towards the suction side. This high momentum jet is highly modified by the concave curvature of the carved surface near the suction side exit area. The concave curvature of the carved bottom surface provides an upward momentum towards the casing surface, effectively reducing the leakage mass flow rate passing through the suction side rim shows a number of streamlines of the leakage flow entering the tip gap. They are directed towards the cavity. Pressure side arm of the horseshoe vortex originating on the LE top platform impinges on the cavity surface as seen in the figure. Increasing the depth of cavity around the corner of LE and PS will achieve a considerable reduction in the thermal loads. The streamlines generated in Fig. 15 are always started from the exact same set of initial seed points for both flat tip and carved tip. This feature helps to compare the exact trajectory of each streamline passing through the tip gap. Fig. 15 clearly shows the reduction in the area coverage of the tip leakage vortex for the case of carved tip (carved77), forming near the SS corner of the tip airfoil. The carved tip design generates highly disturbed leakage streamlines influenced from the carved cavity's concave shape and its unique recirculatory flow as shown in Fig. 15. The horseshoe vortex like LE vortices cannot stay near the PS corner, generating additional interference with the leakage jet. This vortical system marked in Fig. 15 clearly separates away from the PS rim corner and moves into the carved cavity to produce more mixing and a reduction in overall leakage mass flow rate. This is not the case for the case of flat tip design.

4. Concluding remarks and future work

In this study, a novel blade tip carving design methodology is explored in a parametric approach in order to improve the aerothermal performance of axial turbines. The carved blocks removed from the tip surface are defined using Bezier points. In order to avoid any sharp corners and edges, the height of the carved block is determined to be 0.5 mm surrounding the carving area. NSGA-II genetic algorithm code coupled with a meta model is used to obtain the optimized blade tip design. Artificial Neural Network (ANN), Support Vector Machine (SVM) and Extreme Learning Machine (ELM) are tested as the meta models to be coupled with the optimization code. A database which initially contained CFD solutions for 55 different designs specified using the Sobol design of experiment method is constructed to train the meta models used. In order to test the prediction capabilities of these models, CFD solutions are performed for the designs selected from the Pareto fronts obtained. These solutions are then added to the training database and the optimization process is repeated with this enlarged database.

Among the meta models tested, ELM was found to converge faster than SVM and ANN. However, it was found that ELM had poor prediction capability. Consistent solutions were achieved for both SVM and ANN, and among these two, ANN yielded better predictions.

Carved blade tip designs reduced the total pressure loss coefficient measurably. However, the carved tip designs were not able to reduce the heat transfer coefficient at a great rate below the flat tip levels. An optimized blade tip design "carved77" obtained from the current multi-objective optimization method is analyzed in detail.

Thermal transport in impingement influenced areas are enhanced. Velocity vectors visualized in the middle plane of design "carved77" show that the leakage flow follows the concave cavity surface instead of impinging on it. This type of flow structure is likely to reduce the thermal loads to the compound-curved bottom surface.

The strong concave curvature of this bottom surface provides an upward momentum to the leakage jet moving towards the suction side corner. This additional upward momentum induced by tip carving is one of the reasons for reduced leakage mass flow rate.

The backward facing step originating at the straight LE boundary of the cavity and the leakage jet starting to form near the PS corner combine their influences to define a typical high heat transfer zone.

The streamlines in the tip gap of "carved77" are more three-dimensional and disturbed as they are influenced from the carved cavity's unique concave shape and its resulting recirculatory flow.

The horseshoe vortex like tip flow system of "carved77" cannot stay near the PS corner, all along the PS. This flow structure entering into the carved cavity generates additional interference with the leakage jet and it provides a measurable reduction in the leakage mass flow rate when compared to the flat tip design.

Tip carving related design proposals from this study can be listed as follows:

- The region which will be carved from the blade tip surface should be determined carefully specifically to reduce the heat loads. The LE of the carved block can be shifted towards the blade LE to weaken the vortex pair due to the impingement of the flow over the blade LE.
- Bottom surface of the carved block is crucial for the heat transfer characteristics since the cavities on the surface can create an insulation layer for reducing heat loads.
- The depth of the carved block is critical to prevent the leakage flow re-attaching the surface. Increasing the depth will reduce the strong impingement of the leakage flow on the carved bottom surface.
- Results indicate that it may not be feasible to develop a blade tip design having the best aerodynamic and thermal performance simultaneously. Design specifications result in a decision problem. The designer can introduce weight functions in order to bring a solution to this issue.

Tip carving method carries a great potential in gas turbines since it enables the investigation of undiscovered blade tip geometries resulting in aerothermal performance improvements.

Declaration of Competing Interest

The authors declared that there is no conflict of interest.

Acknowledgments

This research was funded by TAI – Turkish Aerospace Industries Inc. (Grant No. DKT/2014/05). The turbine blade profile used in the exploration of the aero-thermally optimized blade tip design using genetic algorithm belongs to TAI – Turkish Aerospace Industries Inc. The last author C. Camci also thanks to the Pennsylvania State University, Turkey and Istanbul Technical University, Turkey for their generous support during his sabbatical leave.

Appendix A. Supplementary material

Supplementary data to this article can be found online at <https://doi.org/10.1016/j.ijheatmasstransfer.2019.07.069>.

References

- [1] R. Boyle, T. Katsanis, J. Haas, Comparison between measured turbine stage performance and the predicted performance using quasi-3D flow and boundary layer analyses, in: Paper Presented at the 20th AIAA/ASME Joint Propulsion Conference, 1984.

- [2] J.D. Coull, N.R. Atkins, H.P. Hodson, Winglets for improved aerothermal performance of high pressure turbines, *J. Turbomach.* 136 (9) (2014), <https://doi.org/10.1115/1.4026909>, 091007-091007-091011.
- [3] F.J.G. Heyes, H.P. Hodson, G.M. Dailey, The effect of blade tip geometry on the tip leakage flow in axial turbine cascades, *J. Turbomach.* 114 (3) (1992) 643–651, <https://doi.org/10.1115/1.2929188>.
- [4] S.K. Krishnababu, P.J. Newton, W.N. Dawes, G.D. Lock, H.P. Hodson, J. Hannis, C. Whitney, Aerothermal investigations of tip leakage flow in axial flow turbines—part I: effect of tip geometry and tip clearance gap, *J. Turbomach.* 131 (1) (2008), <https://doi.org/10.1115/1.2950068>, 011006-011006.
- [5] G.S. Azad, J.-C. Han, R.S. Bunker, C.P. Lee, Effect of squealer geometry arrangement on gas turbine blade tip heat transfer, *J. Heat Transfer* 124 (3) (2002) 452–459, <https://doi.org/10.1115/1.1471523>.
- [6] N.L. Key, T. Arts, Comparison of turbine tip leakage flow for flat tip and squealer tip geometries at high-speed conditions, *J. Turbomach.* 128 (2) (2004) 213–220, <https://doi.org/10.1115/1.2162183>.
- [7] A.A. Ameri, E. Steinþorsson, D.L. Rigby, Effect of squealer tip on rotor heat transfer and efficiency, *J. Turbomach.* 120 (4) (1998) 753–759, <https://doi.org/10.1115/1.2841786>.
- [8] C. Camci, D. Dey, L. Kavurmacioglu, Aerodynamics of tip leakage flows near partial squealer rims in an axial flow turbine stage, *J. Turbomach.* 127 (1) (2005) 14–24, <https://doi.org/10.1115/1.1791279>.
- [9] P.J. Newton, G.D. Lock, S.K. Krishnababu, H.P. Hodson, W.N. Dawes, J. Hannis, C. Whitney, Heat transfer and aerodynamics of turbine blade tips in a linear cascade, *J. Turbomach.* 128 (2) (2004) 300–309, <https://doi.org/10.1115/1.2137745>.
- [10] S.W. Lee, S.U. Kim, Tip gap height effects on the aerodynamic performance of a cavity squealer tip in a turbine cascade in comparison with plane tip results: part 1—tip gap flow structure, *Exp. Fluids* 49 (5) (2010) 1039–1051, <https://doi.org/10.1007/s00348-010-0848-6>.
- [11] S.W. Lee, M.Y. Choi, Tip gap height effects on the aerodynamic performance of a cavity squealer tip in a turbine cascade in comparison with plane tip results: part 2—aerodynamic losses, *Exp. Fluids* 49 (3) (2010) 713–723, <https://doi.org/10.1007/s00348-010-0849-5>.
- [12] C. Zhou, H. Hodson, Squealer geometry effects on aerothermal performance of tip-leakage flow of cavity tips, *J. Propulsion Power* 28 (3) (2012) 556–567, <https://doi.org/10.2514/1.B34254>.
- [13] C.B. Senel, H. Maral, L.A. Kavurmacioglu, C. Camci, An aerothermal study of the influence of squealer width and height near a HP turbine blade, *Int. J. Heat Mass Transfer* 120 (2018) 18–32, <https://doi.org/10.1016/j.ijheatmasstransfer.2017.12.017>.
- [14] D. Dey, C. Camci, Aerodynamic Tip Desensitization of an Axial Turbine Rotor Using Tip Platform Extensions, 2001, 78507, V001T003A069. doi: 10.1115/2001-GT-0484.
- [15] C. Zhou, H. Hodson, I. Tibbott, M. Stokes, Effects of winglet geometry on the aerodynamic performance of tip leakage flow in a turbine cascade, *J. Turbomach.* 135 (5) (2013), <https://doi.org/10.1115/1.4007831>, 051009-051010.
- [16] J.H. Cheon, S.W. Lee, Tip leakage aerodynamics over the cavity squealer tip equipped with full coverage winglets in a turbine cascade, *Int. J. Heat Fluid Flow* 56 (2015) 60–70, <https://doi.org/10.1016/j.ijheatfluidflow.2015.07.003>.
- [17] N.M. Rao, B. Gumusel, L. Kavurmacioglu, C. Camci, Influence of Casing Roughness on the Aerodynamic Structure of Tip Vortices in an Axial Flow Turbine 4241X (2006) 893–903. doi: 10.1115/GT2006-91011.
- [18] B. Gumusel, Aerodynamic and Heat Transfer Aspects of Tip and Casing Treatments Used for Turbine Tip Leakage Control. (Ph.D.), The Pennsylvania State University, 2008.
- [19] L.A. Kavurmacioglu, C.B. Senel, H. Maral, C. Camci, Casing grooves to improve aerodynamic performance of a HP turbine blade, *Aerosp. Sci. Technol.* 76 (2018) 194–203, <https://doi.org/10.1016/j.ast.2018.01.047>.
- [20] H. Maral, C.B. Senel, L. Kavurmacioglu, A Parametric and Computational Aerothermal Investigation of Squealer Tip Geometry in an Axial Turbine: A Parametric Approach Suitable for Future Advanced Tip Carving Optimizations (49705) (2016) V02BT38A058. doi: 10.1115/GT2016-58107.
- [21] Q. Zhang, L. He, Tip-shaping for HP turbine blade aerothermal performance management, *J. Turbomach.* 135 (5) (2013), <https://doi.org/10.1115/1.4007896>, 051025–051025–051027.
- [22] C. De Maesschalck, S. Lavagnoli, G. Paniagua, Blade tip carving effects on the aerothermal performance of a transonic turbine, *J. Turbomach.* 137 (2) (2014), <https://doi.org/10.1115/1.4028326>, 021005–021005–021010.
- [23] C. De Maesschalck, S. Lavagnoli, G. Paniagua, T. Verstraete, R. Olive, P. Picot, Heterogeneous optimization strategies for carved and squealer-like turbine blade tips, *J. Turbomach.* 138 (12) (2016), <https://doi.org/10.1115/1.4033975>, 121011–121011–121012.
- [24] V. Andreoli, J. Braun, G. Paniagua, C. De Maesschalck, M. Bloxham, W. Cummings, L. Langford, Aerothermal Optimization of Fully Cooled Turbine Blade Tips 51104 (2018) V05CT22A001. doi: 10.1115/GT2018-75099.
- [25] M. Paty, B.C. Cernat, C. De Maesschalck, S. Lavagnoli, Experimental and numerical investigation of optimized blade tip shapes – Part I: tip flow analysis and loss mechanisms, *J. Turbomach.* (2018), <https://doi.org/10.1115/1.4041466>.
- [26] M. Paty, B.C. Cernat, C. De Maesschalck, S. Lavagnoli, Experimental and numerical investigation of optimized blade tip shapes – Part II: tip flow analysis and loss mechanisms, *J. Turbomach.* (2018), <https://doi.org/10.1115/1.4041466>.
- [27] K. Deveci, H. Maral, C.B. Senel, E. Alpman, L. Kavurmacioglu, C. Camci, Aerothermal optimization of squealer geometry in axial flow turbines using genetic algorithm, *J. Therm. Eng.* 4 (3) (2018) 1896–1911, <https://doi.org/10.18186/journal-of-thermal-engineering.408701>.
- [28] K. Deb, A. Pratap, S. Agarwal, T. Meyarivan, A fast and elitist multiobjective genetic algorithm: NSGA-II, *IEEE Trans. Evol. Comput.* 6 (2) (2002) 182–197, <https://doi.org/10.1109/4235.996017>.
- [29] ANSYS CFX 16.0 Introduction to Turbulence: Lecture 10, 2016.
- [30] M. Cavazzuti, *Optimization Methods from Theory to Design Scientific and Technological Aspects in Mechanics*, first ed., Springer-Verlag, Berlin Heidelberg, 2013.
- [31] M.T. Hagan, H.B. Demuth, M.H. Beale, O. De Jesús, *Neural Network Design*, vol. 20, Pws Pub, Boston, 1996.
- [32] C.-C. Chang, C.-J. Lin, {LIBSVM}: A library for support vector machines. *ACM Trans. Intell. Syst. Technol.*, 2011. Retrieved from <<https://www.csie.ntu.edu.tw/~cjlin/libsvm/>>.
- [33] G.-B. Huang, Q.-Y. Zhu, C.-K. Siew, *Extreme learning machine: theory and applications*, *Neurocomputing* 70 (1–3) (2006) 489–501.
- [34] Retrieved from <<https://www.gnu.org/software/octave/>>.